Analysis and modeling of momentum transport based on NBI modulation experiments at ASDEX Upgrade

C. F. B. Zimmermann[a][b][*], R. M. McDermott[a], E. Fable[a], C. Angioni[a],
B. P. Duval[d], R. Dux[a], A. Salmi[c], U. Stroth[a][b], T. Tala[c], G. Tardini[a],
T. Pütterich[a], and the ASDEX Upgrade[e] and MST1[f] experimental teams

[a] *Max Planck Institute for Plasma Physics, 85748 Garching, Germany*
[b] *Physik-Department E28, Technische Universität München, 85747 Garching, Germany*
[c] *VTT, P.O. Box 1000, FI-02044 VTT, Finland*
[d] *Ecole Polytechnique Fédérale de Lausanne, Swiss Plasma Center, CH-1015 Lausanne, Switzerland*
[e] *see the author list of H. Meyer et al. 2019*
[f] *see the author list of B. Labit et al. 2019*

[*] E-mail of the corresponding author: benedikt.zimmermann@ipp.mpg.de

Abstract

The prediction of the plasma rotation is of high interest for fusion research due to the effects of the rotation upon MHD instabilities, impurities, and turbulent transport in general. In this work, an analysis method was studied and validated to reliably extract momentum transport coefficients from NBI modulation experiments. To this end, a set of discharges was created with similar background profiles for the ion and electron temperatures, the heat fluxes, the electron density, and the plasma rotation that, therefore, should exhibit similar momentum transport coefficients. In these discharges, a range of temporal perturbations were imposed by modulating and varying the power deposition of the NBI, ECRH, and ICRH. The transport model including diffusion, convection, and residual stress was implemented within the ASTRA code. The Prandtl number $Pr = \chi_\varphi/\chi_i$ was assessed via the GKW code. A convective Coriolis pinch was fitted and the intrinsic torque from the residual stress was estimated. The obtained transport coefficients agree within error bars for sufficiently small imposed temperature perturbations, as would be expected, from the similar background profiles. This successful validation of the methodology opens the door to study the parametric dependence of the diffusive and convective momentum transport of the main ions of the plasma as well as the turbulent intrinsic torque in a future work.

1 Introduction

1.1 Motivation

The study of momentum transport is needed to understand turbulent transport and to provide reliable predictions for the performance of tokamak plasmas. In particular, a validated understanding of momentum transport is required to predict the toroidal rotation profile, which has a strong impact on other processes, particularly

on neoclassical [1] and impurity transport [2–6]. Sufficient rotation can provide stability against neoclassical tearing modes [7, 8], resistive wall modes [9–11], and locked mode instabilities [12]. By the velocity shear, rotation can stabilize turbulence and influence the confinement [13–17]. Despite this relevance, there is currently no fully validated predictive model for the plasma rotation. Predicting the plasma rotation requires knowledge of all major sources, sinks, and momentum transport coefficients. Moreover, whereas heat transport can be described as purely diffusive process [18–23] and particle transport by a combination of diffusion and convection [24–26], momentum transport requires the additional inclusion of a residual stress. Residual stress is a turbulent transport component that can spin up the core plasma from rest [27]. This phenomenon is connected with the off-diagonal terms of the transport matrices, which play a bigger role in momentum transport [28] than in heat or particle transport. To provide a consistent model of the momentum transport, it is necessary to understand the dependence of this residual stress on plasma parameters, its localization, and how it will scale to a future reactor plasma. The aim of this work is to develop and validate an experimental method to uniquely, separately, and concomitantly determine the contribution of diffusion, convection, and residual stress to momentum transport within the core plasma. In particular, this work focuses on the analysis and interpretation of neutral beam injection (NBI) modulation experiments in ASDEX Upgrade.

1.2 Review

Modulation experiments are commonly used to study transport in fusion plasmas. The technique has been used for heat and particle transport experiments [29], where, in the case of particle transport, it can separate the diffusive and convective fluxes. For momentum transport, the technique is more challenging, as one must not only separate the diffusive and convective fluxes, but also any residual stress. With NBI as the actuator to induce a momentum perturbations, there is an additional and undesired side effect of a simultaneous heat perturbation that can impact the ion heat conductivity, χ_i. Previous NBI modulation experiments used a variety of techniques, assumptions, and simplifications to analyze the experimental data. Recent works do not provide a validation of a methodology to uniquely separate all three contributions to the momentum transport in tokamak plasmas.

At JET, NBI modulations experiments were analyzed by Tala *et al.*, where theoretical predictions and experimental observations for the momentum diffusion and inward convection, also called pinch, were found to be in good qualitative agreement. Significant momentum convection was needed to explain the experimental data [30, 31]. In a more detailed study in 2011 [32], Tala *et al.* investigated the parametric dependencies of the momentum diffusion and convection by comparing discharges from JET with gyrokinetic simulations. These experiments are similar to those in this work, having NBI modulation with turbulent transport dominated by ion-temperature-gradient (ITG) driven modes. Both in theory and experiment, a strong dependence of the momentum convection on the density gradient was found. In a multi-machine comparison, Tala *et al.* [33] were able to study the parameter dependence of convection and diffusion coefficients utilizing NBI modulation and non-resonant magnetic field perturbation (NRMP) techniques. In all four works, [30–33], they were unable to clearly separate the effect of the residual stress and do not consider the transport coefficients to change in time.

Tardini *et al.* also studied JET discharges with NBI modulation and modelled

the momentum transport [34]. They were able to separate convective and diffusive contributions, but neglected the residual stress. Weisen *et al.* [35] analyzed the non-diffusive momentum transport in JET via a database approach only focusing on the steady-state profiles of the rotation, which does not allow separating possible effects of a residual stress from the convection.

In a recent work at the KSTAR tokamak, Yang *et al.* [36] emphasize the need to retain a time dependent reaction of the transport coefficients to changing plasma parameters in such an analysis when the perturbation amplitudes become large. They found that large amplitude perturbations in T_i and χ_i, e.g. NBI modulation, can lead to artificially high momentum transport coefficients. This also can play a role when the ICRH is used to modulate T_i independently without a concurrent momentum drive, resulting in independent modulation amplitudes of T_i and v_φ as seen in the experiments analyzed here, which requires the calculation of heat and momentum diffusivities as a function of time. This was also underlined by Camenen *et al.* who demonstrated the strong influence of small turbulence modulations on the reconstruction of momentum transport coefficients [37]. The authors conclude that, especially in NBI modulation experiments, full time dependence in the transport coefficients while solving the momentum transport equation has to be kept.

Yoshida *et al.* applied beam modulation techniques using the perpendicular neutral beam injection at JT-60U [38, 39]. The toroidal field ripple causes fast ion losses, leading to a modulation of the toroidal rotation. Their results suggested an inward momentum flux that was not consistent with either a diffusive flux or the Coriolis momentum pinch. In a later work, Yoshida *et al.* studied momentum transport via the transient transport analysis of L-H transitions [40]. Using off-axis, near perpendicular beams, the external torque is negligible. They separated the convection and diffusion and included residual stress in their analysis, which improved the modelling accuracy of the experimental data significantly.

In Alcator C-Mod Rice *et al.* found strong toroidal rotation even in absence of an external torque. In these works, the different transport components could not be separated [41, 42], but the presence of an inward momentum pinch was indicated [43]. Alcator C-Mod also investigated the momentum transport by studying the L-H transition [44]. They found strong evidence for inward momentum convection in H-mode plasmas. In a recent paper, Rice *et al.* performed a multi-machine parameter dependence study including their data from Alcator C-Mod comparing the plasma rotation before and after L-H and L-I transitions [45]. The authors find scaling laws for the intrinsic torque from the residual stress and extrapolate it to ITER, again, without separating transport components.

Significant work was carried out at DIII-D, utilizing the ability to provide neutral injection with opposing beams capable of balanced effective momentum input. In multiple papers, de Grassi *et al.* conclude that there must be a significant intrinsic rotation present [46, 47], also in the pedestal region [48]. Recently, Chrystal *et al.* predicted the intrinsic rotation in ITER, based on empirical scaling laws for DIII-D [49].

Also Solomon *et al.* investigated momentum transport at DIII-D [50]. In this work they focus on steady-state analysis by balancing the residual stress with the NBI torque. Via torque scans and extrapolation, they estimate the size of the intrinsic rotation caused by an anomalous torque. They conclude that the residual stress cannot be neglected in momentum transport studies. In another work, Solomon *et al.* were utilizing non-resonant magnetic fields and NBI beam blips [51]. The au-

thors identified the need for significant inward momentum pinch in order to explain the experimental results, suggesting that a purely diffusive ansatz was not sufficient. In experiments with balanced beams they found a substantial residual stress, resulting in significant co-current intrinsic rotation. In 2011, Solomon *et al.* examined the intrinsic rotation [52], focusing more on the edge of the plasma. The authors neglected the time dependence of the momentum diffusion in contrast to this work, where time-dependent coefficients are used.

McDermott *et al.* investigated the core momentum transport in ASDEX Upgrade based on a large database [53]. They used the GS2 code [54] to provide theoretical estimates for the convection and diffusion. Based on the steady-state toroidal rotation profiles they solved for the residual stress. The analysis of discharges in TEM turbulence regime suggested that residual stress drives counter-current toroidal rotation of the order of that driven by the NBI. In a later work [55], they expanded their database with a large number of Ohmic L-mode plasmas and studied the transition from linear to saturated Ohmic confinement. This study showed that the density gradient provides the dominant dependence of the residual stress in the core of ASDEX Upgrade, but that collisionality, and the ion temperature gradient, also contribute.

1.3 Outline

One can conclude that to accurately model momentum transport, one needs to account for all three components: diffusion, convection, and residual stress. In particular, the diffusion term must be modelled as a function of time. NBI modulation experiments are the method of choice, since they can discriminate the different transport coefficients with full time dependence without changing the underlying momentum transport provided the perturbation is sufficiently small. A validated methodology for such analysis must also be constructed.

To this end experiments were performed in 2017 at AUG in which a range of perturbations using NBI, ECRH and ICRH were applied to an otherwise identical background H-mode plasma. The analysis of this data set should demonstrate that our methodology is capable of reproducing the same transport coefficients for these identical background profiles regardless of what kind of perturbation was applied.

This paper is laid out as follows. In Section 2 the theoretical models are introduced together with their optimization to fit the experimental data. Then, in Section 3, the performed experiments are discussed. Section 4 presents the momentum transport coefficients and the intrinsic torque from the residual stress is estimated. Lastly conclusions are drawn and next steps discussed.

2 Momentum Transport Modelling

2.1 Basic equations

Due to the toroidal symmetry of a tokamak plasma, the toroidal angular momentum is a conserved quantity and can be described by a toroidal momentum conservation equation [56]

$$m_i \frac{\partial}{\partial t} n_i \langle R v_\varphi \rangle = -\frac{1}{V'} \frac{\partial}{\partial \rho} V' \Gamma_\varphi + \langle R \rangle S_{\text{NBI}} \quad (1)$$

with the torque density of the NBI, S_{NBI}, the main ion density n_i and mass m_i, the flux surface averaged local major radius $\langle R \rangle$, and the toroidal velocity v_φ. The

radial flux of toroidal momentum Γ_φ can be expressed as

$$\Gamma_\varphi = -m_i n_i R_0^2 \langle |\nabla\rho|^2\rangle (\chi_\varphi \frac{\partial}{\partial\rho}\frac{v_\varphi}{R} - \frac{V_c v_\varphi}{R} + \Pi_{\mathrm{Rs}}) \tag{2}$$

where the first term in the brackets is the diffusive momentum flux given by the momentum diffusivity χ_φ multiplied by the gradient of the toroidal flow. The second term describes the convective flux, denoted by the product of a convective velocity V_c and the toroidal velocity itself. The last term, $m_i n_i R_0^2 \langle|\nabla\rho|^2\rangle \Pi_{\mathrm{Rs}}$, is the residual stress. $\langle|\nabla\rho|^2\rangle$ is a geometrical term due to the shape of the tokamak. Eq. 2 is a flux surface averaged quantity, and, since poloidal flows are neglected within the formalism presented here, the flow on a flux surface can be approximated by solid body rotation, namely $\omega = v_\varphi/R$, which is consequently also constant on magnetic flux surfaces and only radially dependent [57, 58]. Eq. 1 and 2 are combined to give the total expression for transport of angular momentum conservation used in this work:

$$m_i \frac{\partial}{\partial t} n_i \langle R v_\varphi\rangle = \frac{1}{V'}\frac{\partial}{\partial\rho}V' m_i n_i R_0^2\langle|\nabla\rho|^2\rangle (\chi_\varphi\frac{\partial}{\partial\rho}\frac{v_\varphi}{R} - \frac{V_c v_\varphi}{R} + \Pi_{\mathrm{Rs}}) + \langle R\rangle S_{\mathrm{NBI}}. \tag{3}$$

2.2 Analysis workflow

In steady state, the time derivative in Eq. 3 vanishes (l.h.s. $\rightarrow$ 0), reducing this equation to a balance of applied external torque, in this case from NBI, diffusive and convective fluxes, and the residual stress. The externally applied torque is, generally, well known. Using a purely steady-state analysis results, therefore, in one equation with three unknown components, and an inability to uniquely identify the individual coefficients.

By retaining the time dependence, and introducing small perturbations to the angular momentum via the NBI power modulation, the observed propagation of the modulation allows the momentum transport coefficients and the residual stress to be separated. It should be noted that the time dependencies of almost all quantities (n_i, v_φ, χ_φ, V_c, S_{NBI}) are tracked in this work, with the exception of the residual stress, which is, at present, assumed to be constant in time. Maintaining its time dependence is the subject of future work.

In this work, some simplifications have been applied. The charge exchange recombination spectroscopy (CXRS) is used to measure the impurity rotation and in this work the impurity rotation is assumed to reflect the main ion rotation. The neoclassical flows [59] have been calculated using the NEOART code [60, 61] and the main ion toroidal rotation is expected to be higher than the impurity rotation by on average 7.5 km/s within the range of interest of $0.2 < \rho_\varphi < 0.8$. Here, ρ_φ is the normalized square root of the toroidal flux, defined as $\rho_\varphi = \sqrt{(\Psi_0 - \Psi)(\Psi_0 - \Psi_{sep})}$ with Ψ_0, the toroidal flux along the magnetic axis ($r = 0$), and Ψ_{sep} at the separatrix. Including the deviation of the measured impurity rotation from the modelled main ion rotation is an additional complication that may be considered in future work.

The first step to solve Eq. 3 is to calculate the torque from the NBI by the NUBEAM code via the TRANSP framework [62–64]. NUBEAM uses a Monte Carlo approach to calculate the total applied torque from the neutral beams as well as the fast ion velocity distribution. Within TRANSP, the ion and electron heat fluxes, Q_i and Q_e, are calculated. To this end, a number of experimental profiles and quantities are required.

The experimental data for the toroidal rotation v_φ and the ion temperature T_i is assessed with charge exchange spectroscopy [65, 66]. The electron density n_e and temperature T_e are obtained via the Integrated Data Analysis [67], based on lithium beam emission spectroscopy [68], the laser interferometry [69], the measurement of the electron cyclotron emission (ECE) radiometry and Thomson scattering [70]. The impurity density profiles n_{imp} [71] and Z_{eff} [72] are obtained directly from CXRS and the measured Bremsstrahlung background, respectively. They are used to estimate the main ion density profiles that are not directly measured.

All experimental data is fitted and pre-processed before it is used in this analysis. The fitting is performed with a bivariate spline fit from the Python-package scipy [73] (`scipy.interpolate.RectBivariateSpline`) with both, radial and temporal smoothing. The radial fitting aims to remove non-physical changes in gradients that result from noise in the measurements. They must be removed to obtain smooth χ_i and χ_e profiles. The condition for the temporal smoothing was to reproduce the Fourier profiles of the first harmonic of the modulation, such that no modulation information is lost. The second harmonic of the modulation is presently not explicitly maintained. Also temporal drifts of background profiles are included, but effects like ELMS ($f_{\mathrm{ELM}} \approx 65...75$ Hz) and sawteeth ($f_{\mathrm{ST}} \approx 60$ Hz) are filtered.

For the NUBEAM calculations, 200,000 particles were simulated to achieve statistically meaningful profiles. The simulation was carried out with a high temporal resolution of 1 ms to resolve the rise time of the fast ions from the NBI as accurately as possible.

All of the fitted profiles as well as the fluxes and the torque from TRANSP are then used by ASTRA [74, 75]. This 1.5D tokamak transport code numerically solves the strongly coupled set of heat and momentum transport Eqs. [56, 76]. ASTRA allows us to solve for the momentum flux in Eq. 3 to calculate χ_φ, V_c, and the residual stress. The advantage of ASTRA is that it is relatively easy to implement different models for the terms in the momentum transport equation.

2.3 Momentum transport model

In this work, a variety of assumptions are tested and a physics-based model is developed to constrain the simulations. Referring to Eq. 3, the diffusive flux is considered firstly. The diffusion coefficient χ_φ and the ion heat conduction coefficient

$$\chi_i = -\frac{Q_i}{n_i \nabla T_i} \tag{4}$$

define the Prandtl number [77]

$$Pr = \frac{\chi_\varphi}{\chi_i}. \tag{5}$$

The Prandtl number is predicted to be of order of unity [27, 78], that is, roughly, confirmed by experiments of several machines [32, 33, 35, 79–82]. χ_φ and χ_i are expected to be strongly coupled as they are proportional to different moments of the same velocity distribution [83, 84]. Also similar ion and momentum confinement times [48, 80] are measured. Thus, theory, supported by experiment, provides a strong constraint on the Prandtl number. By rewriting the diffusive part of the momentum transport equation in terms of the Prandtl number, this constraint can be applied to the simulation.

Several models for the Prandtl number were tested including constant and linearly depending on the radial flux coordinate. A linear ansatz for the Prandtl

number fits the data slightly better and theoretical predictions [85] indeed suggest such a radial dependence. Therefore, within this work, a radially, linearly increasing Prandtl number with two unknowns, $Pr = a + b\,\rho_\varphi$, is assumed.

One contribution to the convective flux (see right hand side of Eq. 2) is the Coriolis momentum pinch, which couples density and temperature perturbations with the parallel velocity moment leading to a radial gradient of the toroidal velocity profile, even in absence of a torque. The physics behind the Coriolis momentum flux is discussed in detail in a number of different publications [28, 86–90]. In Peeters *et al.* [86], the theoretical parameter dependence of the pinch number $-RV_c/\chi_\varphi$ was explored via linear gyrokinetic simulations. It was predicted to vary most strongly with the logarithmic density gradient $R/L_{n_e} = -\frac{R}{n_e}\nabla_r n_e$, the shear s, and the safety factor q. Based on the dependencies found by Peeters *et al.*, within this work, a linear ansatz for the convection given by

$$V_c = -\frac{\chi_\varphi}{R}(\texttt{C1} \cdot \frac{R}{L_{n_e}} + \texttt{C2} \cdot s) \tag{6}$$

is used. As q and s are strongly coupled, only one is included. Possible dependencies on other parameters are, at present, neglected. From theory, parameters $\texttt{C1}$ and $\texttt{C2}$ are positive scalars resulting in negative inward convection, strengthening the existing toroidal rotation [27, 86]. Hence, for AUG, which typically features co-current toroidal rotation at the plasma edge, even in absence of beams, the Coriolis pinch results in an inward flux of co-current momentum.

The last part of the modeling of the momentum transport equation concerns the residual stress Π_{Rs}. This gives rise to an intrinsic torque density S_{int} causing an intrinsic rotation. In contrast to the pinch, it can spin-up the plasma from rest [27]. The effect involves all sources of momentum flux that result from symmetry breaking of turbulence structures that are not proportional to the rotation nor its gradient. Also, wave-particle momentum exchange [27] contributes to this effect. For ITG mode turbulence, the residual stress is expected to act in the co-current direction [27], whereas it was seen to act in the counter-current direction for the trapped-electron mode (TEM) turbulence regime [53]. From global, non-linear gyrokinetic turbulence simulation the effects of the profile shearing have been identified as the dominant contribution to the intrinsic toroidal rotation in the core of AUG [91]. Within this work, the impact of residual stress is included as an additional unknown torque density described by a simple quadratic function and referred to in the following as "intrinsic" torque density, which is the negative divergence of the residual stress $S_{\text{Rs}} = -m_i n_i \langle R \rangle \nabla \cdot \Pi_{\text{Rs}} = a + b\rho_\varphi + c\rho_\varphi^2$. Implementing a physical model is left for the future.

2.4 Fitting methodology

Accounting for S_{NBI}, χ_φ, V_c, and Π_{Rs} with these models and solving the momentum transport equation reduces to fitting the Prandtl number Pr, the free parameters $\texttt{C1}$ and $\texttt{C2}$ in Eq. 6 and in estimating the intrinsic torque density S_{int} from the residual stress. This is performed by solving the momentum transport in ASTRA to predict v_φ and minimizing against the experimentally measured steady-state rotation profile and the radial profiles of the amplitude and phase of the first harmonic of the modulated rotation. This focuses on effects in the core, neglecting the edge, where the experimental values of the toroidal rotation at $\rho_\varphi = 0.8$ are used as a boundary

condition for ASTRA. To avoid redistribution of particles by sawteeth, the region of interest in the analysis is set to $0.2 < \rho_\varphi < 0.8$.

A first attempt to simultaneously fit the diffusion and convection ignoring the residual stress, as was done in previous works, leads to unstable solutions, underlining the need for a third component. The outward diffusion and inward convection counteract for the peaked rotation profiles generally obtained in NBI heated AUG H-mode plasmas. For a given value of Pr, it was possible to find a pinch that reproduced the data equally well. This is demonstrated in Fig. 1 for the reference discharge in our data set #34027, presented in Section 3, using constant $(Pr(r) = C)$ profiles. The experimental phase profiles, here, and in all other plots in this work, are shifted to the average value of the modelled phase profile to emphasize the gradient of the phase and to avoid numerical artifacts arriving with the 2π periodicity of the Fourier coefficients.

Here, and in general, when fitting the diffusion and convection there was a tendency of the pinch to not converge, but rather to grow continually to improve the fit of the convex curvature of the experimentally measured steady-state rotation profiles. No combination of diffusion and convection is able to reproduce that curvature and simultaneously match the measured phase profile. The marginal improvement in the steady state comes at the cost of worsened agreement with the phase. This inability to match the curvature is a clear sign of residual stress that needs to be included. In general, it remains possible that in other plasmas this effect may not be present, but a method that can be arbitrarily applied to a large data set must include it. An advanced fitting approach, including residual stress, should be able to account for this curvature. Additionally, changes in the minimization constraints that place more emphasis on the amplitude and phase profiles can be considered.

A possible solution to this problem, published by Yang *et al.* [36], is to ignore residual stress with a preliminary fit on the phase profile of the toroidal rotation with a constant Prandtl number followed by fitting the pinch to the amplitude and steady-state rotation profile. The assumptions the authors made is that diffusivity has the largest influence on the phase profile. However, in simulations of AUG, it was observed that an isolated fitting of the Prandtl number to the phase profiles leads to an overestimated amplitude profile. The following fit of the pinch then only yields a trivial, zero, solution for the pinch, as any inward pinch would increase the amplitude profile further, increasing the deviation from the experimental profiles. Furthermore, it underestimates the Prandtl number, which would increase for a larger pinch. In conclusion, for the AUG data set analysed herein, this isolated fitting approach of the phase profile is insufficient and such a methodology of [36] is not applicable. A next-generation version of the used methodology including the residual stress directly would remove the problem, but this is not yet included in this work.

Instead, the gyrokinetic flux tube code GKW was used to determine the Prandtl number. GKW simulates instabilities and turbulent transport and considers effects of kinetic electrons, electromagnetic effects, collisions, MHD equilibria coupling of the geometry, and E × B-shearing [92, 93]. Calculations were performed for the reference discharge and their results were applied to all other discharges of the data set, since as previously mentioned, the background profiles and equilibria are identical, within error bars, for all analyzed discharges. The fluxes were weight averaged over a spectrum of five binomial wavenumbers $0.2 < k_y \rho_i < 0.8$. The values of $R\,V_c/\chi_i$ and $R\,V_c/\chi_\varphi$ are obtained for different radial positions, where V_c
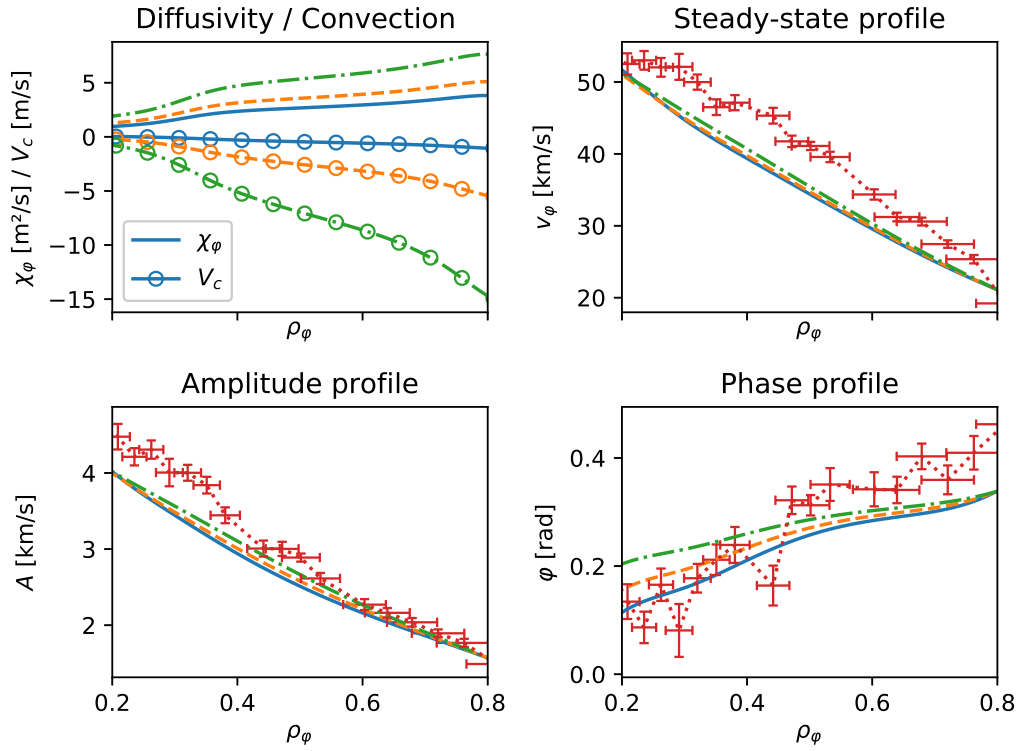
Figure 1: The calculated momentum diffusivity for $Pr = 0.75$ (blue, solid line), $Pr = 1$ (orange, dashed line), and $Pr = 1.5$ (green, dash-dotted line) and the corresponding optimized convection for the reference discharge #34027. One can clearly see the incremental improvement in the steady-state and amplitude profiles of the rotation with increasing Prandtl number. When fitting, the pinch increases trying to fill the gap between the modelled and measured steady-state profile (red, dotted lines). This degeneracy indicates a missing component in this calculation.
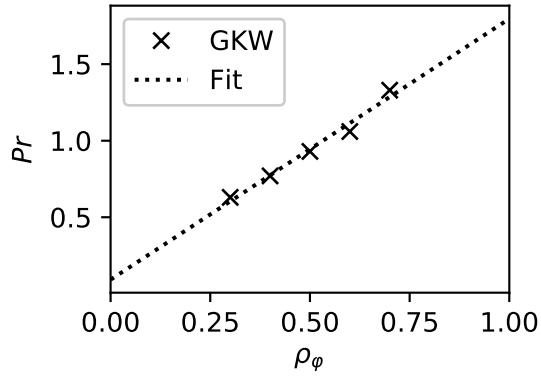
Figure 2: Prandtl number predicted by GKW for the reference discharge #34027

is the convective velocity. The Prandtl number can be assessed as

$$Pr = \chi_\varphi/\chi_i = \left(\frac{R V_c}{\chi_i}\right) \cdot \left(\frac{\chi_\varphi}{R V_c}\right). \tag{7}$$

A linear fit of the results (see Fig. 2) yields

$$Pr(\rho_\varphi) \approx 0.1 + 1.7\,\rho_\varphi. \tag{8}$$

From the pinch number, $-R V_c/\chi_\varphi$, also a pinch velocity

$$V_c = \frac{\chi_{i,turb}}{R} \cdot \left(\frac{R V_c}{\chi_i}\right) \tag{9}$$

can be calculated with the major radius R and the turbulent part of the heat diffusivity $\chi_{i,turb} = \chi_i - \chi_{\mathrm{neo}}$ taken from the TRANSP runs. The predicted pinch will, later in this work, be compared with the fitted pinch number (see Fig. 10). To assess the accuracy of the GKW predictions, one can directly use the diffusion and convection from GKW in an ASTRA simulation. Fig. 3 shows that the amplitude profile is only slightly underpredicted and that, although the phase profile slope is not fully captured, the Fourier profiles are modelled reasonably accurately. The steady-state profile is not correct leaving room for improvement, by including residual stress within the model.
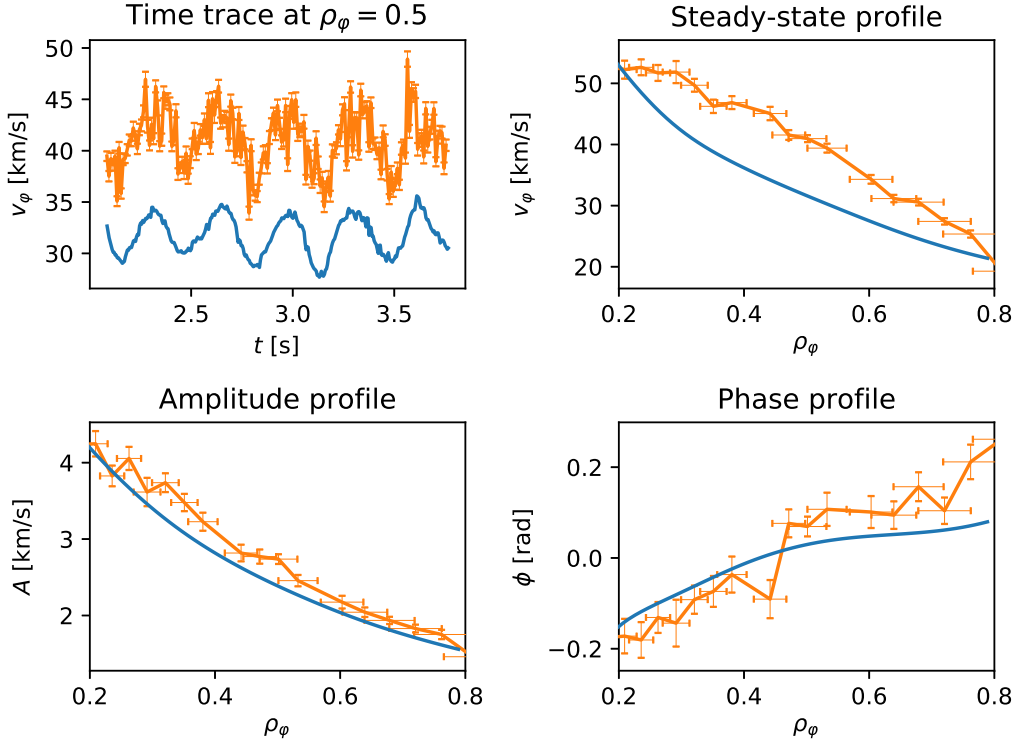
Figure 3: Assessing the prediction from GKW for the convection and diffusion directly in ASTRA for the reference discharge #34027. Experimental Fourier profiles (with error bars) are matched well, but the steady-state profile and time-trace reveal a missing residual stress component in this calculation.

The entanglement of diffusion and convection was resolved by using the linear Prandtl number fit of the GKW prediction (see Eq. 8) for all further calculations in this work. The Prandtl number was preferred over the pinch number, since the Prandtl number is the more robust prediction. The choice of a linear ansatz is not only supported by the prediction. It allows much more flexibility in fitting scenarios where the dominating turbulence regime varies over radius. The feasibility of separating the three transport mechanisms is not affected in the work presented here, because the Prandtl number is fixed to the aforementioned predictions. However, the benefit of this additional degree of freedom, increasing computational costs, has to be assessed carefully in future work.

After having studied the entanglement of convection and diffusion, a similar degeneracy was observed between the residual stress and the convection, where both influence the steady-state rotation profile and the modulation amplitude profile of the rotation. Models of the residual stress [56, 94] include time-dependent quantities such as the diffusivity χ_φ, which cause the residual stress to modulate and so influence the Fourier profiles. To resolve this entanglement, the intrinsic torque due to the residual stress is considered to be constant in time and is optimized to fit the steady-state rotation profile, after the amplitude and phase have been fitted by the diffusion and convection terms. This hierarchy in fitting is justified, as numerical experiments show that the impact of the diffusion and pinch on the Fourier pro-

files is stronger than the effect of the residual stress. In particular, this approach reduces the dimensions of the numerical fitting problem and, thus, computational costs. However, as there is a small influence of a time-dependent residual stress on the Fourier profiles, including it in future work requires the fitting of all three transport components simultaneously. The obtained results will deviate from the ones extracted with the more simple ansatz taken here.

3   Experiment Description

All discharges analyzed in this work were performed under standard conditions: type I ELMy H-mode plasmas with a toroidal field of $B_\varphi = 2.5$ T, a plasma current of $I_p = 0.8$ MA, and a lower single null configuration with an outer plasma position of $R_{\text{out}} = 2.15$ m to provide optimal conditions for the CXRS diagnostics. All discharges had identical background heating and consequently, similar plasma parameters. Figs. 4 and 5 show an overview of the time traces and the kinetic profiles of the reference discharge. The R/L_{n_e}- and shear-profile in Fig. 5 act as basis functions for the fitting of the pinch as they are the main dependency of Eq. 6. They provide a wide range of possible pinch profiles.   All discharges used in this analysis feature identical T_i, T_e, and n_e profiles to within error bars. To these similar background plasmas, different heating perturbations were applied, varying P_{tot} between 6.6 and 7.2 MW. In all cases, a NBI modulation with a frequency of either 3 or 7 Hz was used, which is sufficiently slow compared to the 10 ms acquisition time of the rotation measurements that the modulation cycle can be resolved to a degree that it does not limit the separation of the transport terms. In cases with 3 Hz modulation, the duty cycle was asymmetric in order to obtain stronger effect of higher harmonics of the modulation frequency in the Fourier analysis. In the reference discharge #34027 and at mid-radius, the modulation amplitude of the second harmonic (≈ 0.2 km/s) is only 40 % of the modulation amplitude of the first harmonic (≈ 0.53 km/s) in the symmetrically modulated 7 Hz phases, while in the asymmetrically modulated 3 Hz cases, the second harmonic amplitude (≈ 0.88 km/s) is roughly 60 % of the modulation amplitude of the first harmonic (≈ 1.48 km/s). However, the use of this higher-harmonic data is left for future work.

AUG has two neutral beam injectors, separated toroidally by $180°$ with four sources each. The two injectors provide deuterium particles with main energies of 60 keV (box 1, sources 1-4) and 93 keV (box 2, sources 5-8), when operated at full voltage. In these experiments sources 5 and 6 were used as modulation sources and were operated at reduced voltage of 50 keV to minimize the induced temperature and torque perturbation, except for one case at 60 keV that was used to probe the influence of increasing the modulated power. To heat and to provide neutrals for the CXRS measurements, steady NBI with $P_{\text{NBI}} = 4.8$ MW was also applied. In addition, 0.6 MW of ECRH was applied to avoid tungsten accumulation [95, 96].

An overview of all of the experiments is given in Tab. 1, here divided into 3 subsets. In order to verify the experimental method, experiments with a range of actuator modulations and frequencies were performed. In the first subset, the modulating beam geometry, power and frequency was changed. In the second and third subset, the ECRH and ICRH were modulated.

The first discharge of Subset 1 is the reference discharge #34027, which was carried out with 3 and 7 Hz modulation, using a radial beam with on-axis deposition. Figs. 6a and 6b show the resulting Fourier profiles of the rotation in orange compared
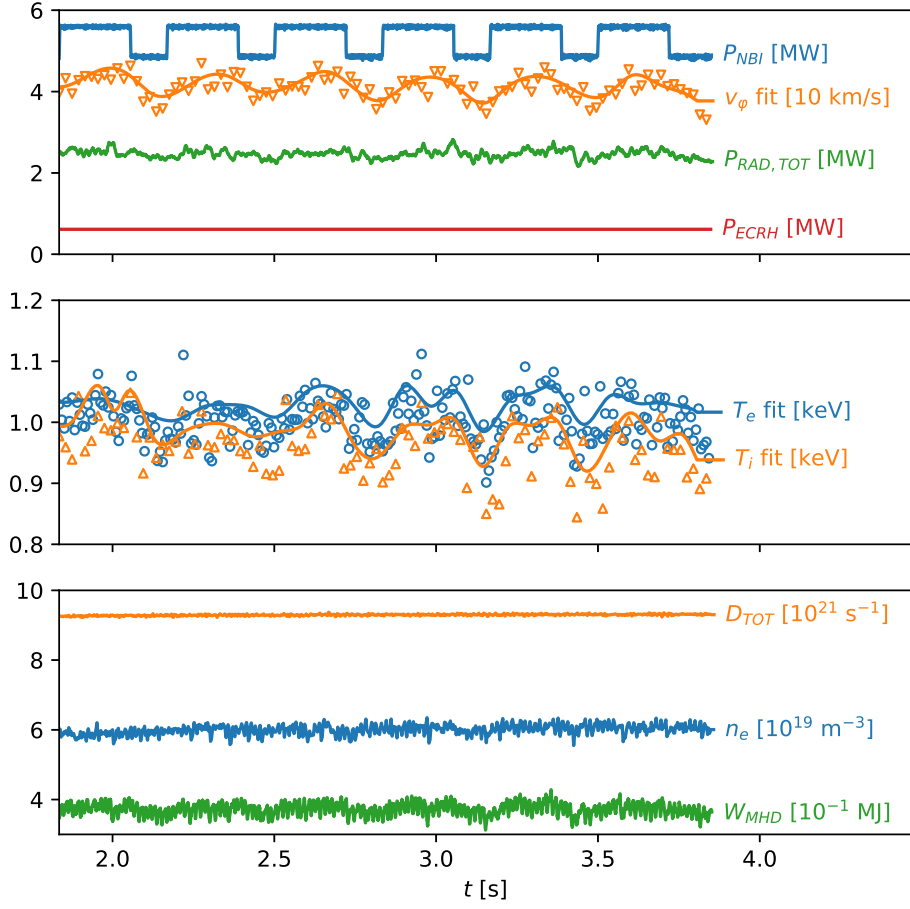
Figure 4: Overview of the reference discharge #34027 at $f_{\mathrm{mod}} = 3$ Hz. The NBI power is modulated, while the density, the ECRH and the radiated power are stable. The stored energy of the plasma exhibits slight modulation. The modulation of the temperatures, although visible, is much lower as that of the rotation.
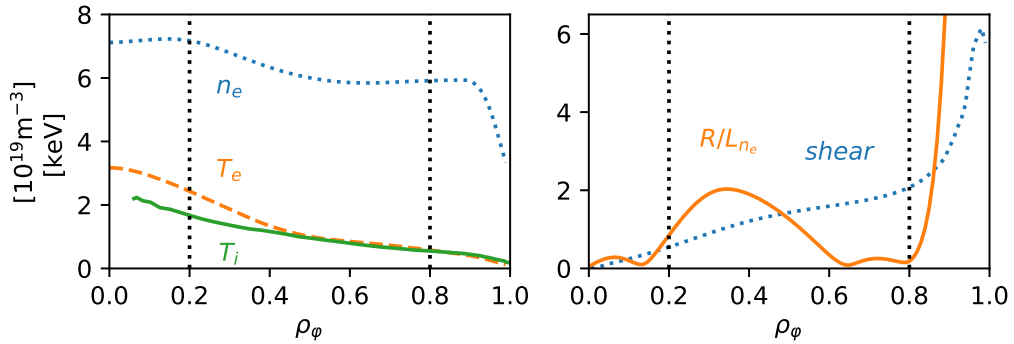

Figure 5: Relevant profiles of the reference discharge #34027 ($f_{\mathrm{mod}} = 3$ Hz), averaged over the time windows. The density profile is very flat in the outer half of the plasma, in contrast to the monotonously increasing shear $s = \frac{\partial q}{\partial r}$ with the safety factor q.
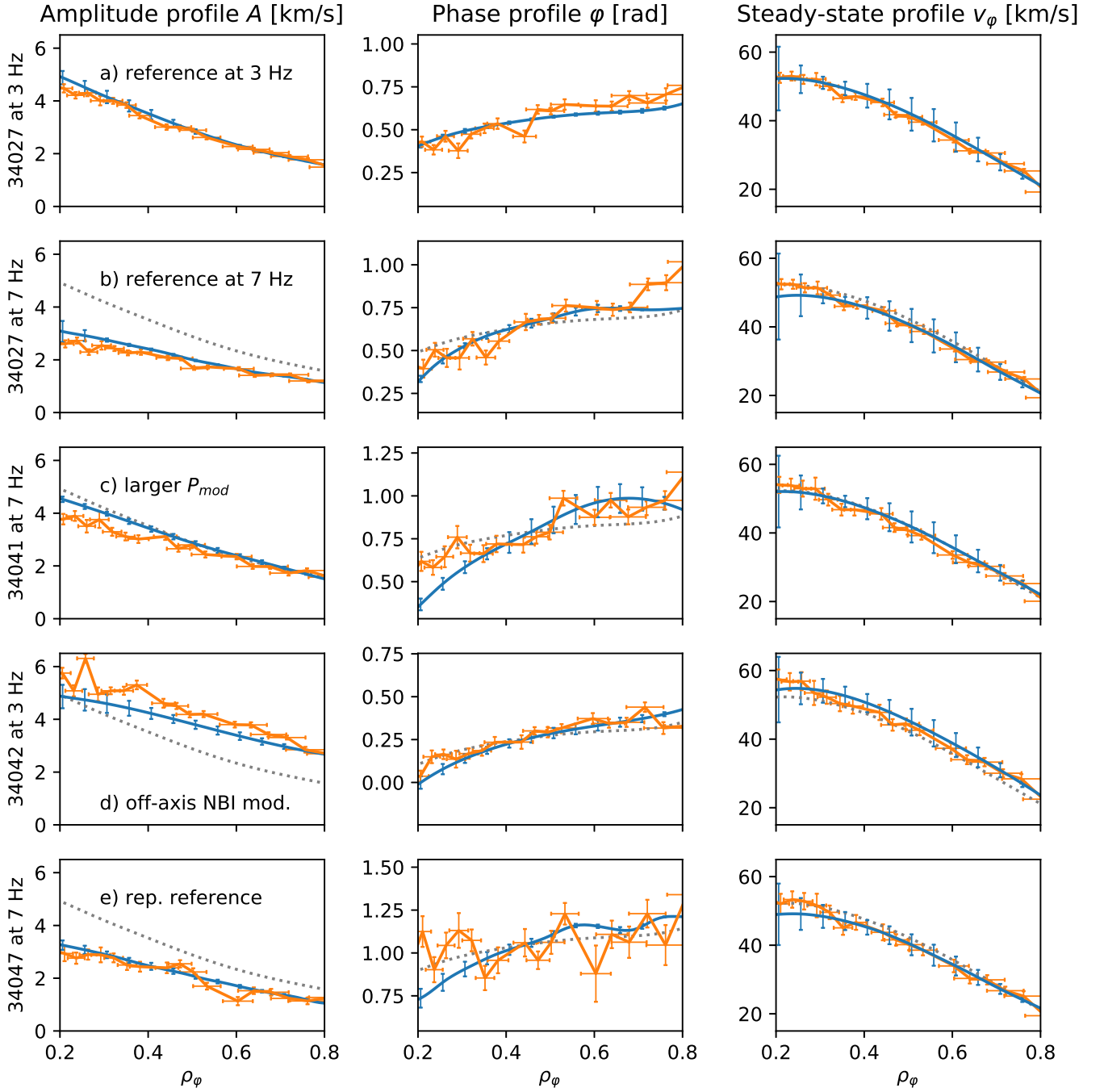
13

Figure 6: Fourier and steady-state profiles of the rotation velocity of selected discharges of Subset 1: ASTRA simulation (**blue**) are compared with experimental data (**orange**). Modulation frequency (b), power (c), and NBI geometry (e) are changed to asses the effects on the modulation of the rotation velocity. The reproducibility is tested in (e). In b) to e), the modelled profiles of the reference discharge #34027 at 3 Hz modulation are shown (**dotted**) to simplify comparison.
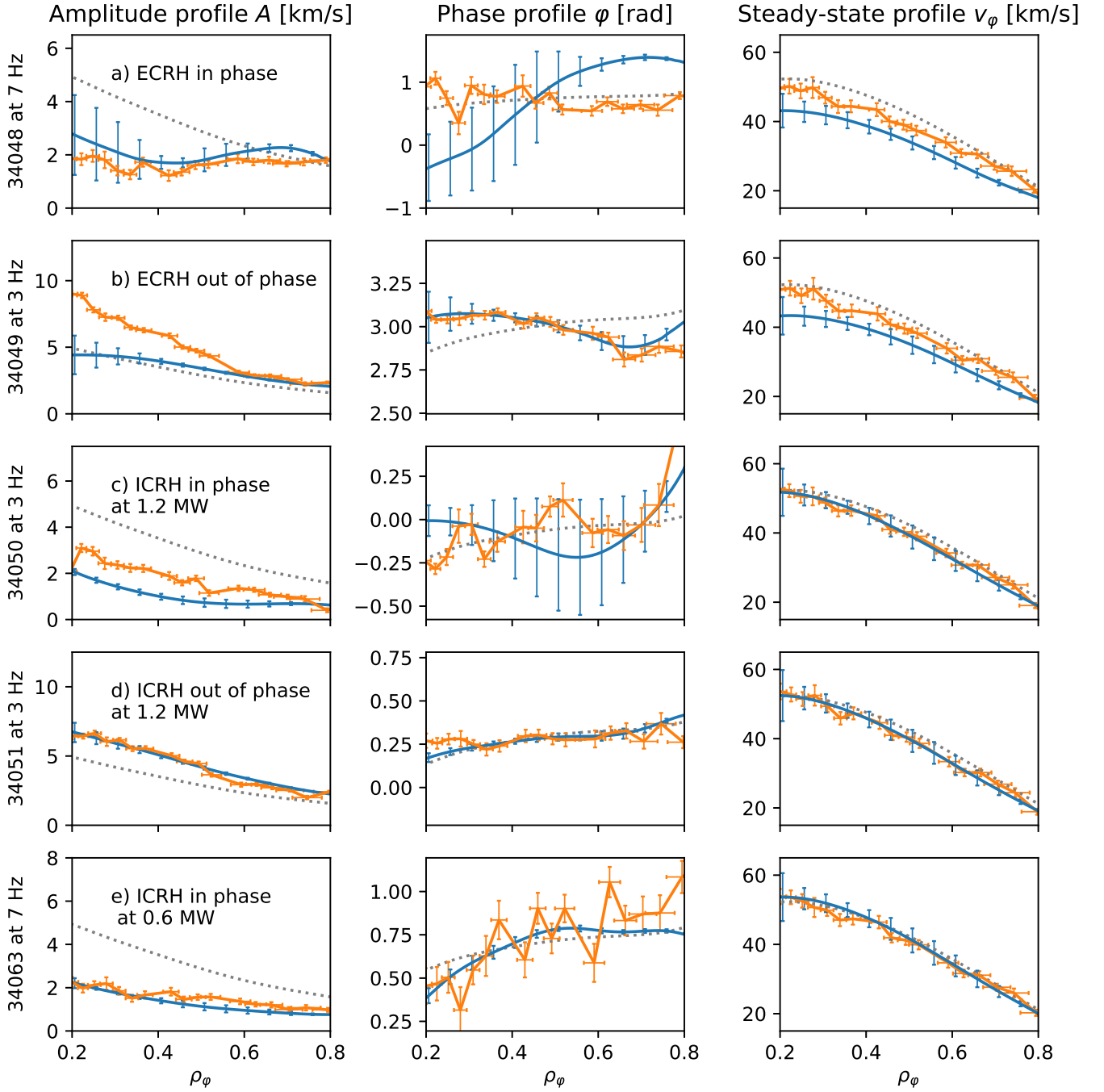
Figure 7: Fourier and steady-state profiles of the rotation of selected discharges of Subset 2 and 3, ASTRA simulation (**blue**) compared with experimental data (**orange**). ICRH and ECRH power are modulated in- and out-of-phase with the NBI modulation to understand the interaction of the heat transport channels with the momentum transport. The modelled profiles of the reference discharge #34027 at 3 Hz modulation are shown (**dotted**) to simplify comparison.

15

Fig.	#	f_{mod} [Hz]	P_{mod} [MW]	NBI	ICRH/ECRH modulation	
6a	34027	3	0.7	on-axis	none	
6b	34027	7	0.7	on-axis	none	
6c	34041	7	1.05	on-axis	none	
6d	34042	3	0.7	off-axis	none	Set 1
	34042	7	0.7	off-axis	none	
	34047	3	0.7	on-axis	none	
6e	34047	7	0.7	on-axis	none	
7a	34048	7	0.7	on-axis	ECRH in phase, 1.2 MW	Set 2
7b	34049	3	0.7	on-axis	ECRH out of phase, 1.2 MW	
	34049	7	0.7	on-axis	ECRH out of phase, 1.2 MW	
7c	34050	3	0.7	on-axis	ICRH in phase, 1.2 MW	
	34050	7	0.7	on-axis	ICRH in phase, 1.2 MW	
7d	34051	3	0.7	on-axis	ICRH out of phase, 1.2 MW	Set 3
	34051	7	0.7	on-axis	ICRH out of phase, 1.2 MW	
	34062	7	0.7	on-axis	ICRH in phase, 0.6 MW	
	34063	3	0.7	on-axis	ICRH out of phase, 0.6 MW	
7e	34063	7	0.7	on-axis	ICRH in phase, 0.6 MW	

Table 1: The variation of modulation frequency, NBI geometry and heating power are given for all discharges analyzed in this work. Subset 1 is without additional RF heating modulation. In Subset 2 and 3, the ECRH and ICRH are used in various configurations to test the influence of changes in the electron and ion heat fluxes on the momentum transport analysis.

to the reference discharge #34027 at 3 Hz modulation as a dashed line and the results of the modelling, shown in blue, which will be discussed in the next section. The case with higher frequency has a lower amplitude and a steeper phase profile, as expected. In discharge #34041, the 7 Hz phase of the reference discharge was repeated with a higher beam voltage. Here, 10 and 12.5 Hz modulation were tested, but resulted in modulation profiles that were too noisy to be useful. The higher beam voltage results in a slight increase in the modulation amplitude as shown in Fig. 6c (to be compared with the reference discharge at 7 Hz, Fig. 6b). In discharge #34042, the reference discharge was repeated with off-axis modulation. The total deposited torque is shown on the r.h.s. in Fig. 8, compared with on-axis modulation. The broader distribution of the off-axis heating results in a higher, but slightly flatter amplitude profile as shown in Fig. 6d. To test experimental reproducibility, #34047 is an exact repeat of the reference discharge performed on a different day with possibly altered wall conditions. This was only partly successful, as shown in Fig. 6d, as the repeat phase profile is noisier and flatter. The reason for this is unclear, as all engineering parameters were successfully repeated and the steady-state profiles well reproduced. Overall, discharges of Subset 1 provide different phase and amplitude rotation profiles while preserving the steady-state profiles. All steady-state profiles are within error bars. This is shown in Figs. 6 and 7. The agreement is illustrated by the dotted profile of the reference discharge #34027 at 3 Hz modulation and the experimental data of each discharges to be compared in orange. The modulation of n_e and W_{MHD} are below 1 % in most cases (Fig. 5). The T_i modulation is of the order of 2.5 % at mid-radius and up to 5 % in the core. The heat diffusivities,
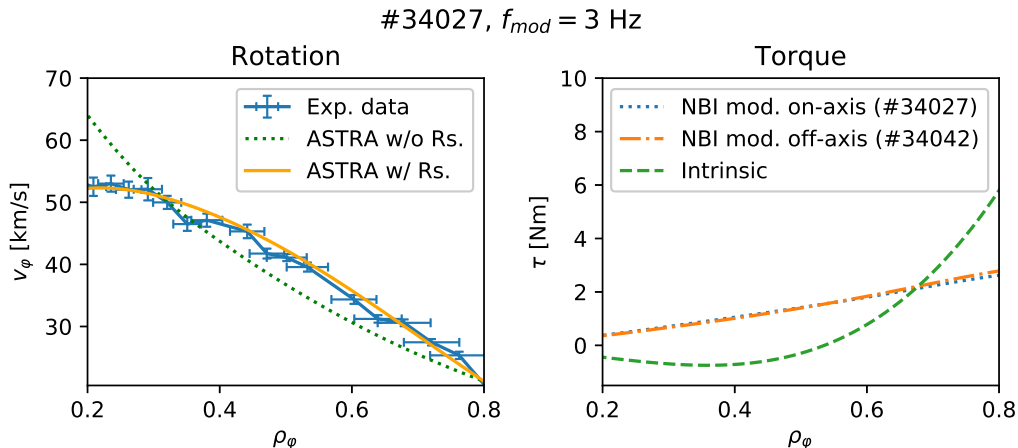
Figure 8: Modelled and experimental rotation velocity profiles of the reference discharge #34027 with diffusion and convection only (l.h.s, orange) and the required intrinsic torque to correct this deviation (r.h.s). For comparison, the NBI torque with on- and off-axis modulation is plotted. Including the intrinsic torque from the residual stress fixes the modelled rotation (l.h.s. green, dotted).

assessed by TRANSP, modulate between $5-10\%$ within Subset 1, already indicating a need to employ diffusivities as a function of time. In general, the agreement of the steady-state profiles supports the assumption that the transport governing this discharges should be very similar, which has to be recovered in the analysis.

To further verify the experimental method, in Subset 2 and 3, the ICRH and ECRH power were modulated in- or out-of-phase of the NBI modulation with a range of power levels in the discharges. This results in a variety of distinct Fourier profiles of the rotation modulation shown in Fig. 7. Fig. 9 shows the timing of the duty cycles of the heating for cases with purely NBI modulation and ICRH modulation in- and out-of-phase with the NBI. The plot illustrates the attempt to minimize (out-of-phase) and maximize (in-phase) the perturbation of the ion heat transport to test their impact upon the momentum transport analysis. In contrast to the first data subset, here, the temperature modulation is no longer always small, #34050 with in-phase ICRH modulation exhibits 15 % modulation of the temperatures. Modulating the ICRH power out-of-phase, #34051, has the opposite effect: the modulation of T_i becomes smaller than in the reference discharge. The impact on T_i is also shown in Fig. 9. These additional RF perturbation can influence the momentum diffusivity in this analysis, since it is coupled to the ion diffusivity via the Prandtl number (see Eq. 5). In discharge #34050, the ICRH was modulated with 1.2 MW in phase with the NBI. This leads to lower amplitude profiles compared with respect to the reference discharge. This is also observed with ICRH modulated with a reduced power of 0.6 MW (see Fig. 7e). In all these cases, again, dependency of the amplitude size and phase steepness on the modulating frequency was observed, with flatter phase profiles for the 3 Hz modulation and lower amplitudes for the 7 Hz modulation.

Focusing on Subset 2, in discharges #34048 and #34049, the ECRH power was modulated by 1.2 MW in- and out-of-phase with the NBI modulation (see Table 1). With ECRH modulating in-phase, both, the phase and the amplitude are flattened,
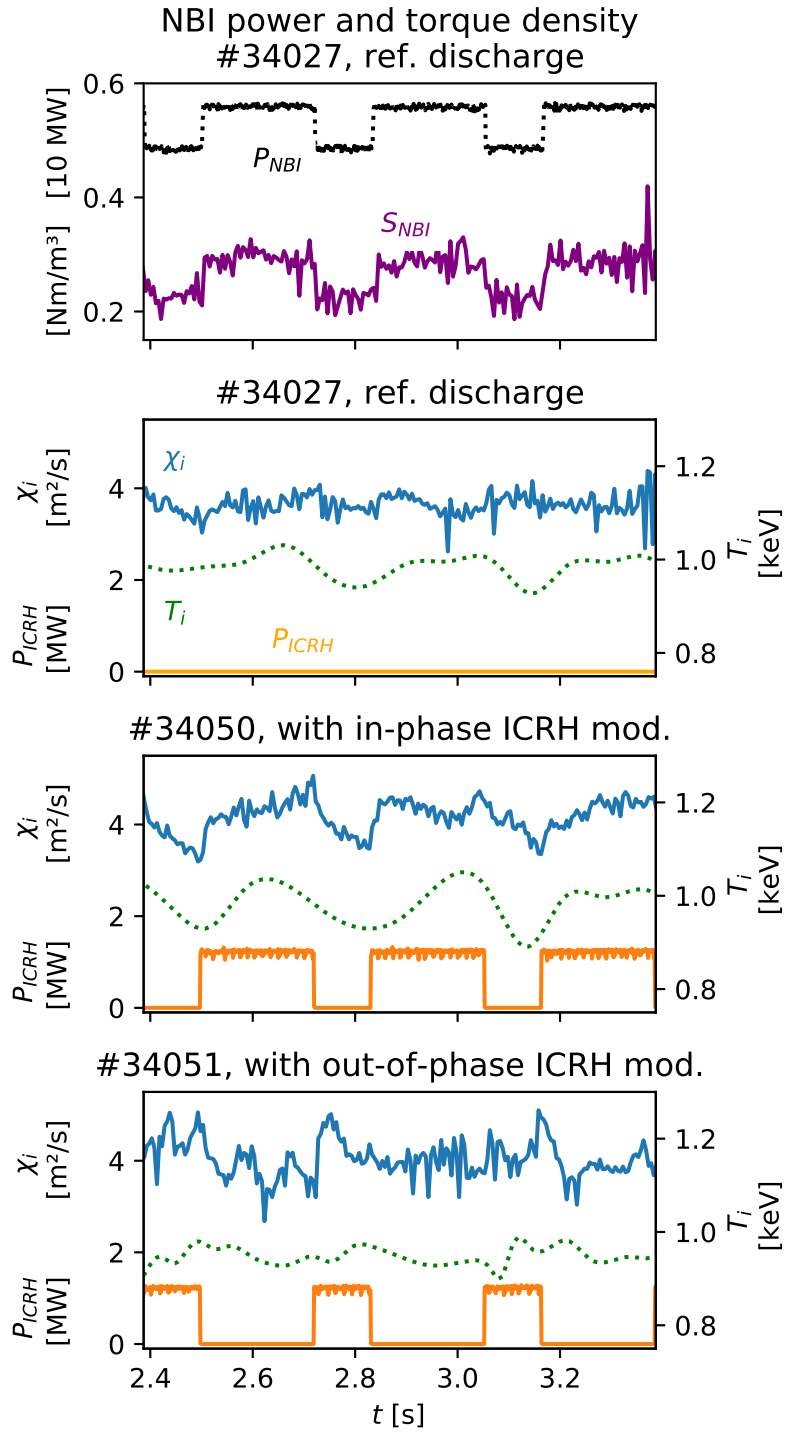
Figure 9: Top: modulation of the NBI power and resulting torque density at mid-radius for 3 Hz modulation taken from the reference discharge #34027. Below: ICRH power, ion temperature and ion heat diffusivity for the reference discharge #34027 without additional RF and discharges #34050 and #34051 with in- and out-of-phase ICRH, respectively.

similar to the ICRH cases. When ECRH is modulated out-of-phase, the rotation amplitude profile increases significantly compared to the reference while the gradient of the phase profile changes sign, what is indicative for a significant change of the transport. Overall, these discharges are more strongly perturbed. Density changes on the order of 3 % at the modulation frequency. Since the particle source is constant, the changes result from changed transport. This suggests that the influence of the heat perturbation is too large to be modelled with the method described herein.

4 Results

The chosen methodology, namely using the linearly increasing Prandtl number from GKW, a two term pinch model, and a constant intrinsic torque was used in the analysis of the set of discharges presented in Table 1. Transport coefficients were obtained for all cases, exhibiting similar background profiles. Of special interest is the comparison of the different NBI modulation frequencies, geometries, and heating configurations and the quality of fits to the phase and amplitude profiles. A successful modelling of the momentum transport and the stability of the fitting against small perturbations is the key to validating the analysis approach.

4.1 Fitting of diffusion and convection

Fitting the free parameters in Eq. 6 to match the experimental steady-state and modulation data of the plasma rotation results in the transport coefficients shown in Fig. 10 for selected cases. These are time-averaged profiles, temporal changes in the diffusion mainly result from modulation of the heating, changes in the pinch number are caused by the R/L_{n_e}-dependence in Eq. 6. The diffusion coefficient and the pinch number of the modelled discharges agree within error bars regardless of frequency, heating geometry, or modulated NBI power amplitude. For the diffusivity, this is to be expected, as the Prandtl number is fixed, the heat fluxes are similar, and the gradients are all the same. Of course, some variation is expected as the perturbed χ_i are not identical: towards the limits of error bars is the increased diffusivity in the discharge with ICRH modulation in-phase (#34050). This could indicate an enhanced transport or a wrong Prandtl number. The error bars are estimated by varying the transport parameter until the deviation from the rotation profiles becomes larger than the error in the fitted experimental data. GKW underpredicts the pinch number, but only by a small margin. However, at this stage, residual stress does not include time dependence in our model, which could alter the modelled amplitude profiles and, thus, influence the fitted pinch.

This first analysis underlines the need to treat the diffusivities as a function of time. As Eq. 3, 4, and 5 suggest, the modulation of Q_i and Q_e via the ECRH and ICRH influences the ion heat diffusivity χ_i. Fourier analysis of χ_i shows that a modulation of ~ 5 % in the reference discharge and up to 15 % in cases with ECRH and ICRH modulation. Fig. 9 shows the corresponding time traces at mid-radius. Such a significant change in χ_i directly affects the momentum diffusion in this model and, from the scaling of Eq. 6, the convection. This clearly influences the modelled Fourier profiles and cannot be neglected.
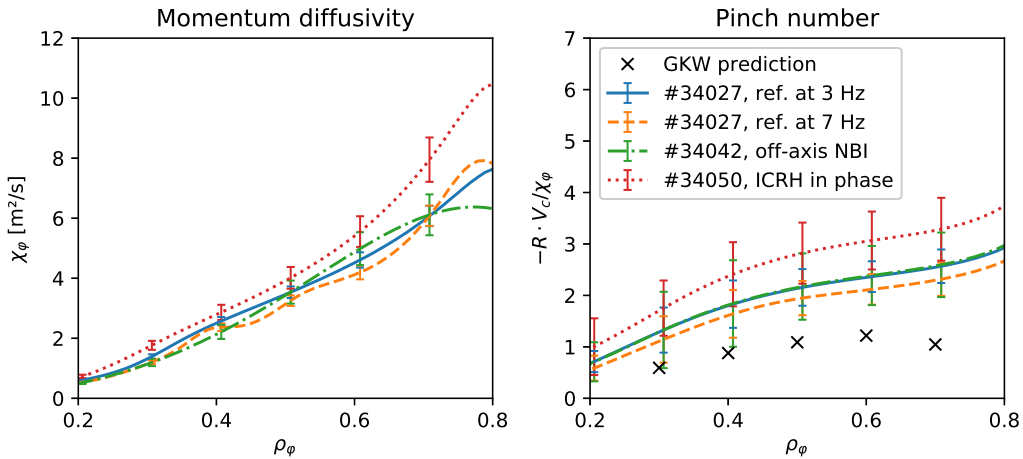
Figure 10: Overview of time-averaged, fitted momentum pinch number and diffusion for similar discharges with different modulation frequencies and heating schemes. The assessed transport parameters are within error bars, the GKW prediction is slightly too low.

Phase and amplitude profiles from the ASTRA modelling of the rotation using the optimized transport profiles and a comparison with the experimental data is shown in Figs. 6 and 7. In Subset 1, without ICRH and ECRH modulation, modelling reproduces the Fourier profiles well for all cases (Fig. 6). The corresponding steady-state profiles will be discussed in Section 4.2 together with the residual stress. Small caveats remains such as the amplitude profiles of the discharges #34041 (higher modulated power, see Fig. 6c), which is slightly overestimated and #34042 (off-axis NBI, see Fig. 6d), which is slightly underestimated.

In the other subsets, with ICRH and ECRH modulation, many of the cases are not well reproduced by the model. For most cases, either the phase and/or the amplitude profile cannot be reconstructed (see Fig. 7). For the discharge from Subset 2 with in-phase ECRH modulation, the phase profile is poorly reproduced (see Fig. 7a), while for out-of-phase ECRH modulation it is the amplitude profile that does not match (see Fig. 7b). Overall, the density and T_e modulation was of the order of a few percent and probably beyond the applicability of this method, even though the density and temperatures are consistently included in the simulation. In principle, the modulation of the electron heating should not severely affect the momentum transport in the model applied here, since the ion temperature and heat diffusivity do not exhibit a strong modulation. This is indicating that the additional heat fluxes were sufficient to alter the turbulence state. In this case, the assumption of using the Prandtl number assessed from the reference discharge would not be applicable.

In discharges of data Subset 3 (#34050 − #34063), the ICRH power was modulated. Subset 3 illustrated the effects of strong perturbation in the ion channel, especially in cases with in-phase ICRH modulation with a modulated power of 1.2 MW. This directly perturbs the momentum transport through $\chi_\varphi = Pr \cdot \chi_i$. Cases with lower modulation of 600 kW are modelled correctly, both, for ICRH modulated power in-phase (maximizing the perturbation in the ion heat channel) and out-of-phase (minimizing the ion heat perturbation). For the purely NBI cases, χ_i

variations up to 10 % were still well captured by the simulations, while for the 1.2 MW ICRH in-phase, where the modulation of χ_i increased to 20 %, the amplitude profiles were no longer reproduced. The size of the perturbation appears to have exceeded the range of applicability for the implemented linear power balance model for the ions and, possibly, a non-linear model for the ion heat transport is needed, as suggested by Yang *et al.* [36]. To investigate this hypothesis, the authors implemented, as an initial test, a non-linear model to solve the power balance for the ion heat transport. This did not improve the agreement. Further exploration of this possibility will be the subject for future work.

4.2   Estimation of the residual stress

The modelled steady-state rotation profiles shows a gap between experimental and modelled rotation demonstrated for the reference discharge on the left hand side of Fig. 8. The sawtooth inversion radii were checked for all analzyed discharges and lay between $0.150 < \rho_\varphi < 0.208$, so the boundary conditions were set correctly and such effects cannot cause the deviation between modelled and experimental data.

It is taken that this gap emerges from residual stress. The intrinsic torque density S_{int} needed to correct the steady-state rotation profile was fitted. This resulted in an intrinsic torque corresponding to approximately one half of the steady-state torque from a single beam at mid-radius (see right hand side of Fig. 8). Then, the intrinsic torque calculated for the reference discharge was used in the simulations of all other discharges which have similar background profiles. This results in correct steady-state rotation profiles for all cases, including these with ECRH and ICRH modulation, as shown in Figs. 6 and 7.

5   Conclusion

In this work, a framework was implemented to study the three components of momentum transport: diffusion, convection, and the residual stress. This method was tested on a data set with various momentum and heating perturbations applied to an, otherwise, identical plasma. To date, the study was limited to plasma dominated by ITG modes, with the assumption of a theoretically predicted, linear Prandtl number and an intrinsic torque that is constant as a function of time.

This paper has attempted to contrast where the model is appropriate and, conversely, where it appears to fail. In data Subset 1, the NBI modulation frequency and deposition profiles were varied, and thus the experimental modulation amplitude and phase profiles of the rotation velocity. The momentum transport of this set of discharges is described by similar transport coefficients, within error bars, validating the methodology under these conditions. However, data Subset 2 showed that if the applied perturbations are large enough to significantly alter the turbulent state, as is the case with high ECRH modulation, then there is no possibility to describe the transport with coefficients derived from unperturbed scenarios. Similar, Subset 3 demonstrated that if the perturbation of χ_i is too large, there will, clearly, be limitations on the use of such a simple model.

Having only one distinct plasma analyzed, this work is far from drawing conclusions about dependencies of the assessed transport coefficients. Furthermore, a direct comparison to investigations at other machines is only valid to a limited extent due to the different methodology and models applied. Nevertheless, a first compari-

son of the order of magnitude of the assessed pinch and intrinsic torque indicates the consistency of the results. Within this work, a radially increasing Prandtl number was calculated via the gyrokinetic code GKW and a pinch and intrinsic torque were found that, with the Prandtl number, reproduced the experimental data. Such a radial increasing Prandtl number of similar size was also experimentally found by Tala *et al.* [32] at JET. In that study, also the pinch was gyro-kinetically simulated and found to underestimate the experimentally determined pinch. There, the experimental pinch is slightly higher than the pinch assessed in this work. Since no residual stress was included in that analysis, further quantitative agreement cannot be expected. A rather recent analysis of JT-60U results finds comparable pinch and diffusion as in this work [97]. The order of magnitude and shape of the intrinsic torque found here agree with investigations at DIII-D [50, 52]. In addition, the shape and size of the assessed intrinsic rotation are comparable with results of studies carried out before at AUG [55].

As a result of this work, flexible tools are prepared and methodology is validated to use NBI modulation as an experimental technique to assess all three momentum transport components with a variety of different models. In future work they will be applied on a large data set and the authors aim to improve the fitting methodology to simultaneously fit all components with full time dependence without constraining the Prandtl number.

Acknowledgments

References

[1]   F. L. Hinton and S. K. Wong. 1985. *The Physics of Fluids.* 28. 3082–3098.

[2]   C. Angioni et al. 2015. *Physics of Plasmas.* 22. 055902.

[3]   F. J. Casson et al. 2014. *Plasma Physics and Controlled Fusion.* 57. 014031.

[4]   F. J. Casson et al. 2013. *Nuclear Fusion.* 53. 063026.

[5]   C. Angioni et al. 2012. *Physics of Plasmas.* 19. 122311.

[6]   C. Angioni et al. 2014. *Nuclear Fusion.* 54. 83028.

[7]   P. A. Politzer et al. 2008. *Nuclear Fusion.* 48. 075001.

[8]   R. J. Buttery et al. 2008. *22nd IAEA Fusion Energy Conference.*

[9]   E. J. Strait et al. 1995. *Phys. Rev. Lett.* 74. 2483–2486.

[10]   A. M. Garofalo et al. 2002. *Phys. Rev. Lett.* 89. 235001.

[11]   H. Reimerdes et al. 2007. *Phys. Rev. Lett.* 98. 055001.

[12]   P. C. de Vries et al. 2011. *Nuclear Fusion.* 51. 053018.

[13]   H. Biglari et al. 1990. *Physics of Fluids B: Plasma Physics.* 2. 1–4.

[14]   T. S. Hahm. 1994. *Physics of Plasmas.* 1. 2940–2944.

[15]   T. S. Hahm and K. H. Burrell. 1995. *Physics of Plasmas.* 2. 1648–1651.

[16]   K. H. Burrell. 1997. *Physics of Plasmas.* 4. 1499–1518.

[17]   P. W. Terry. 2000. *Rev. Mod. Phys.* 72. 109–165.

[18]   X. Garbet et al. 2004. *Plasma Physics and Controlled Fusion.* 46. B557–B574.

[19]   P. Mantica et al. 2019. *Plasma Physics and Controlled Fusion.* 62. 014021.

[20]   F. Ryter et al. 2001. *Phys. Rev. Lett.* 86. 5498–5501.

[21]   F Ryter et al. 2003. *Nuclear Fusion.* 43. 1396–1404.

[22]   F. Ryter et al. 2011. *Nuclear Fusion.* 51. 113016.

[23]   F. Ryter et al. 2019. *Nuclear Fusion.* 59. 096052.

[24]   C. Angioni et al. 2009. *Plasma Physics and Controlled Fusion.* 51. 124017.

[25]   D. R. Baker et al. Apr. 1998. *Nuclear Fusion.* 38. 485–494.

[26]   K. W. Gentle et al. Feb. 1992. *Nuclear Fusion.* 32. 217–237.

[27]   P. H. Diamond et al. 2009. 49. 045002.

[28]   C. Angioni et al. 2012. *Nuclear Fusion.* 52. 114003.

[29]   N. J. Lopes Cardozo. 1995. *Plasma Physics and Controlled Fusion.* 37. 799–852.

[30]   T. Tala et al. 2007. *Plasma Physics and Controlled Fusion.* 49. B291–B302.

[31]   T. Tala et al. 2009. *Phys. Rev. Lett.* 102. 075001.

[32]   T. Tala et al. 2011. *Nuclear Fusion.* 51. 123002.

[33]   T. Tala et al. 2012. *24th IAEA Fusion Energy Conference.*

[34]   G. Tardini et al. 2009. *Nuclear Fusion.* 49. 085010.

[35]   H. Weisen et al. 2012. *Nuclear Fusion.* 52. 042001.

[36]   S. M. Yang et al. 2018. *Nuclear Fusion.* 58. 066008.

[37]   Y. Camenen et al. 2017. *44th EPS Conference on Plasma Physics.*

[38]   M. Yoshida et al. 2007. 47. 856–863.

[39]   M. Yoshida et al. 2009. *Nuclear Fusion.* 49. 115028.

[40]   M. Yoshida et al. 2012. *Nuclear Fusion.* 52. 023024.

[41]   J. E. Rice et al. 2008. *Plasma Physics and Controlled Fusion.* 50. 124042.

[42]   J. E. Rice et al. 2011. *Phys. Rev. Lett.* 106. 215001.

[43]   J. E. Rice et al. 2004. *Nuclear Fusion.* 44. 379–386.

[44]   W. D. Lee et al. 2003. *Phys. Rev. Lett.* 91. 205003.

[45]   J. E. Rice et al. 2021. *Nuclear Fusion.* 61. 026013.

[46]   J. S. DeGrassie et al. 2004. *Physics of Plasmas.* 11. 4323–4331.

[47]   J. S. DeGrassie et al. 2007. *Physics of Plasmas.* 14. 056115.

[48]   J. S. DeGrassie et al. 2009. *Nuclear fusion.* 49. 085020.

[49]   C. Chrystal et al. 2020. *Nuclear Fusion.* 60. 036003.

[50]   W. M. Solomon et al. 2007. *Plasma Physics and Controlled Fusion.* 49. B313.

[51]   W. M. Solomon et al. 2009. *Nuclear Fusion.* 49. 085005.

[52]   W. M. Solomon et al. 2011. *Nuclear Fusion.* 51. 073010.

[53]   R. M. McDermott et al. 2011. *Plasma Physics and Controlled Fusion.* 53. 035007.

[54]   M. Kotschenreuther et al. 1995. *Computer Physics Communications.* 88. 128–140.

[55]   R. M. McDermott et al. 2014. *Nuclear Fusion.* 54. 043009.

[56]   E. Fable. 2015. *Plasma Physics and Controlled Fusion.* 57. 045007.

[57]   A. Lebschy et al. 2017. *Nuclear Fusion.* 58. 026013.

[58]   F. L. Hinton and R. D. Hazeltine. 1976. *Reviews of Modern Physics.* 48. 239.

[59]   Y. B. Kim et al. 1991. *Physics of Fluids B: Plasma Physics.* 3. 2050–2060.

[60]   E. Viezzer et al. 2013. *Nuclear Fusion.* 54. 012003.

[61]   A. G. Peeters. 2000. *Physics of Plasmas.* 7. 268–275.

[62]   R. J. Hawryluk. 1981. *Physics of Plasmas Close to Thermonuclear Conditions.* 19–46.

[63]   J. Breslau et al. 2018. *Princeton Plasma Physics Laboratory (PPPL), Princeton, New Jersey, United States.*

[64]   A. Pankin et al. 2004. *Computer Physics Communications.* 159. 157–184.

[65]   E. Viezzer et al. 2012. *Review of Scientific Instruments.* 83. 103501.

[66]   R. M. McDermott et al. 2017. *Review of Scientific Instruments.* 88. 073508.

[67]   R. Fischer et al. 2010. *Fusion Science and Technology.* 58. 675–684.

[68]   R. Fischer et al. 2008. *Plasma Physics and Controlled Fusion.* 50. 085009.

[69]   A. Mlynek et al. 2010. *Review of scientific instruments.* 81. 033507.

[70]   H. Murmann et al. 1992. *Review of Scientific Instruments.* 63. 4941–4943.

[71]   R. M. McDermott et al. 2018. *Plasma Physics and Controlled Fusion.* 60. 095007.

[72]   R. Fischer et al. 2010. *37th EPS Conference on Plasma Physics.*

[73]   P. Virtanen et al. 2020. *Nature Methods.* 17. 261–272.

[74]   G. Pereverzev and P. N. Yushmanov. 2002. *Max Planck Institute for Plasma Physics, Garching, Germany.*

[75]   E. Fable et al. 2013. *Plasma Physics and Controlled Fusion.* 55. 124028.

[76]   A. A. Ivanov et al. 2005. *Proceedings of 32nd EPS Conference on Plasma Physics.* 29. 5–63.

[77]   D. Strintzi et al. 2008. *Physics of Plasmas.* 15. 044502.

[78]   P. H. Diamond et al. 2008. *Physics of Plasmas.* 15. 012303.

[79]   P. C. de Vries et al. 2006. *Plasma Physics and Controlled Fusion.* 48. 1693–1708.

[80]   P. C. de Vries et al. 2008. *Nuclear Fusion.* 48. 065006.

[81]   J. S. DeGrassie et al. 2003. *Nuclear fusion.* 43. 142.

[82]   S. D. Scott et al. 1990. *Phys. Rev. Lett.* 64. 531–534.

[83]   N. Mattor and P. H. Diamond. 1988. *The Physics of Fluids.* 31. 1180–1189.

[84]   J. Weiland et al. 2007. *Plasma Physics and Controlled Fusion.* 49. A45–A57.

[85]   A. G. Peeters and C. Angioni. 2005. *Physics of Plasmas.* 12. 072515.

[86]   A. G. Peeters et al. 2007. *Physical Review Letters.* 98. 265003.

[87]   T. S. Hahm et al. 2007. *Physics of Plasmas.* 14. 072302.

[88]   A. G. Peeters et al. 2009. *Physics of Plasmas.* 16. 062311.

[89]   A. G. Peeters et al. 2009. *Physics of Plasmas.* 16. 042310.

[90]   A. G. Peeters et al. 2011. *Nuclear Fusion.* 51.

[91]   W. A. Hornsby et al. 2018. *Nuclear Fusion.* 58. 056008.

[92]   A. G. Peeters et al. 2009. *Computer Physics Communications.* 180. 2650–2672.

[93]   A. G. Peeters and D. Strintzi. 2004. *Physics of Plasmas.* 11. 3748–3751.

[94]   Y. Camenen et al. 2011. *Nuclear Fusion.* 51. 073039.

[95]   C. Angioni et al. 2017. *Nuclear Fusion.* 57. 056015.

[96]   J. Stober et al. Oct. 2003. *Nuclear Fusion.* 43. 1265–1271.

[97]   Y. Ohtani et al. 2021. *AIP Advances.* 11. 085306.